



Intra- and Cross-View Enhancement for OCTA Imaging

Jingbo Zeng^{1†*}, Bingyao Tan^{2,3†}, Zaiwang Gu⁴, Shenghua Gao¹, Leopold Schmetterer^{2,3}, and Jun Cheng⁴  

¹ The University of Hong Kong, Hong Kong, China
zengjingb@connect.hku.hk

² Singapore Eye Research Institute, Singapore National Eye Center, Singapore, Singapore

³ Duke-NUS Medical School, Singapore, Singapore
bingyao.tan@duke-nus.edu.sg

⁴ Institute for Infocomm Research, A*STAR, Singapore, Singapore
cheng_jun@i2r.a-star.edu.sg

Abstract. Optical coherence tomography angiography (OCTA) is an indispensable modality in ophthalmic imaging, providing high-resolution visualization of retinal microvasculature. Recently, deep learning approaches have been explored to reconstruct OCTA images; however, significant challenges persist, particularly the reliance on high-quality target data for model training, which is often impractical due to limitations in hardware and acquisition protocols. In this work, we present a novel pipeline for deep learning-based OCTA imaging from repeated OCT B-scans, circumventing the need for high-quality training labels. We introduce an Intra-View Enhancement (IVE) module together with a novel loss function Cross-View Matching (CVM) to improve the imaging. The proposed pipeline is evaluated on a local dataset, demonstrating a relative improvement of 4.97% and 27.42% in PSNR and CNR over state-of-the-art learning-based OCTA method respectively. Our results underscore the effectiveness and clinical viability of the proposed approach for OCTA images, highlighting its potential to advance imaging capabilities in challenging clinical environments.

Keywords: Optical Coherence Tomography Angiography · Intra-View Enhancement · Cross-View Matching · Noisy Label

1 Introduction

Optical coherence tomography angiography (OCTA), a contrast-free functional extension of OCT, has emerged as a pivotal medical imaging tool for microvascular visualization and analysis [7],[29]. Conventional OCTA employs decorrelation-based analysis of repeated B-scans to differentiate vascular flow signals from

* The work was done during an internship at I²R, A*STAR.

† Co-first authors

static tissue components, which is highly dependent on handcrafted filters to analyze temporal variations. Current technical approaches encompass several distinct methodologies. Correlation mapping OCT [6] utilizes temporal correlation analysis to enhance microvascular contrast through static or dynamic tissue discrimination. Doppler OCT [31] quantifies flow velocity through phase shift detection in sequential scans. Split-spectrum techniques demonstrate divergent implementations. Split-Spectrum Amplitude-Decorrelation Angiography [11] relies on amplitude decorrelation metrics, whereas Split-Spectrum Amplitude-Phase Gradient Angiography [16] integrates phase gradient analysis to optimize slow-flow detection sensitivity, providing great performance in reducing motion artifacts. Optical Microangiography (OMAG) [26,27] enhances the resolution of vascular imaging through the overlap of B-scan acquisition protocols, achieving a superior spatial sampling density. These methods require multiple repeated scans to obtain an enhanced optimal image quality. Due to inevitable motion, current commercial machines often adopt four overlapping scans to reduce noise.

Recent advances in learning have expanded the scope of OCTA image generation. Lee *et al.* [13] employed a symmetric autoencoder to reconstruct OCTA images from repeated B-scans, while a texture-guided U-Net [34] with Euclidean distance loss improved image quality. Liu *et al.* [18] leveraged repeated scans at identical locations, integrating low-noise targets to improve the signal-to-noise ratio. The introduction of 3D GANs further refined image translation; Li *et al.* [15] converted repeated OCT B scans into 3D volumes and proposed vessel promoted guidance and heuristic contextual guidance modules to improve quality and flow consistency. However, imperfect labeling remains a challenge. The susceptibility to noise significantly complicates the acquisition of training data and influences the performance of the model, presenting a critical barrier to practical implementation. Jiang *et al.* [12] addressed this with a weakly supervised approach using the Noise2Noise (N2N) strategy [21] to learn from noisy OCTA images, but with limited reduction in speckle noise.

Beyond providing OCTA from consecutively sampled data, several enhancement denoising algorithms have been developed as plug-and-play modules to enhance image quality. Liu *et al.* decomposed OCTA images into the wavelet domain and separated the signal from the noise based on the Bayesian posterior probability [17]. Zhang *et al.* used a multiple wavelet-FFT approach to reduce motion artifacts [32]. Yang *et al.* utilized shearlet transforms to differentiate tissue and vasculature in 3D volumes [30]. Li *et al.* simplified the optical shadow attenuation model to a linear illumination transformation and adopted an adversarial network to learn the transformation parameters [14]. Ge *et al.* proposed S2Snet [8], a self-supervised network to reduce OCT speckle noise. Ramos-Soto developed the Metaheuristic-Driven Bayesian Speckle Denoising framework to enhance OCTA images through metaheuristic optimization. Ma *et al.* [20] proposed perceptual and low-rank regularized transformer for denoising. Schottenhamml *et al.* introduced an unsupervised denoising algorithm, SSN2V, to distinguish informative and non-informative speckle, preserving sharper image details

[24]. However, these plug-and-play modules are designed for general purposes and are not fully aligned with the specific needs of OCTA imaging.

Motivated by these limitations, we propose a novel pipeline, ICENet, aimed at reduced speckle noise in OCTA imaging. Drawing inspiration from N2N [21], our pipeline is designed to operate without reliance on high quality labels. By leveraging noisy labels, the proposed method substantially reduces data collection requirements, enhancing efficiency and scalability, particularly within clinical environments where obtaining pristine data is challenging. To mitigate the negative effect of noisy data, we propose a novel Intra-View Enhancement (IVE) module to enhance images. We also introduce a novel loss function specifically tailored for learning from noisy labels [25], which enables the network to provide better performance with imperfect data, resulting in improved OCTA imaging. Quantitative evaluations demonstrate that our approach yields significant improvements in image quality, achieving superior reconstruction accuracy. The proposed pipeline generalizes effectively across diverse datasets, underscoring its suitability for a wide range of clinical applications.

Our main contributions can be summarized as follows.

- We propose a novel intra- and cross-view enhancement approach to learn from noisy data for enhanced OCTA imaging.
- By introducing the IVE module, our network effectively handles noise in low-quality training data, leading to improved image clarity, which is crucial for accurate diagnosis and analysis.
- We propose a novel CVM loss function specifically designed for noisy labels, which significantly reduce the speckle noise in OCTA imaging.
- The proposed pipeline demonstrates a 1.64 *dB* or 4.97% improvement in PSNR, 2.80% improvement in SSIM, and 27.42% improvement in CNR over existing learning-based methods in image quality on the local dataset.

2 Methodology

As demonstrated in Fig. 1, our pipeline provides an integral process for reconstructing consecutive B-scans into OCTA images without high-quality training labels. Our model adopts pretrained Swin-UNET [2] as the backbone. The IVE module is introduced to enhance the output, which will be presented in Section 2.1. Meanwhile, a novel CVM loss function is designed to decrease the negative effect of noise on training data in Section 2.2. The implementation details and measurement metrics are provided in Section 2.3.

2.1 Intra-View Enhancement

As depicted in Fig. 1, the IVE module divides the image into smaller, localized blocks. The IVE module involves computing the similarity between these blocks to capture their inherent patterns and structures. The module is designed to improve the representation of features by merging features from the most similar blocks, thereby capturing richer contextual information.

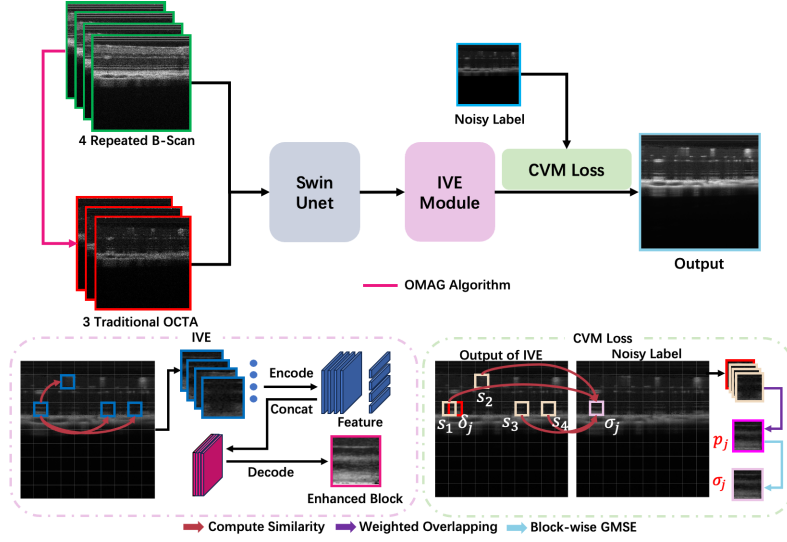


Fig. 1: Overall structure of our proposed ICENet. The proposed ICENet employs Swin-Unet as the baseline together with additional Intra-View Enhancement (IVE) module and Cross-view matching (CVM) loss function. The symbols will be explained in Section 2.2.

For each block, we dynamically select the top- k most similar blocks based on the similarity matrix, where k is an adjustable parameter set to 4 in our experiment, similar to that in BM3D [5]. All blocks undergo an encoding process with the ResNet-18 backbone in which the pixel-level data are transformed into a feature representation. Additionally, the similarity scores for the current block are spatially expanded and concatenated with the features to explicitly incorporate similarity information. These features are concatenated along the channel dimension and passed through a decoder that outputs the enhanced block.

2.2 Cross-View Matching Loss

Loss Function In a supervised network, the mean squared error (MSE) is widely adopted to estimate the difference between the output and ground truth.

$$MSE(f(x_i; \Theta), y_i) = \frac{1}{N} \sum_{i=1}^N \|f(x_i; \Theta) - y_i\|^2, \quad (1)$$

where $f(x_i; \Theta)$ indicates the output, y_i indicates the ground truth, and N stands for the number of pixels.

However, MSE has been shown to be sensitive to outliers or noise in the data [1, 23]. Abundant solutions are presented to handle outliers. Generalized cross entropy (GCE) [33] has been shown to be effective in handling noisy labels and

efficient in model training. With the inspiration of MSE and GCE, we propose a novel loss function called Generalized Mean Squared Error (GMSE).

$$GMSE = \frac{1}{N} \sum_{i=1}^N \frac{(MSE(f(x_i; \Theta), y_i) + \epsilon)^q - 1}{q} = \frac{1}{N} \sum_{i=1}^N \frac{(\|f(x_i; \Theta) - y_i\|^2 + \epsilon)^q - 1}{q}, \quad (2)$$

where ϵ is a small value to keep numerical stability, and $q \in (0, 1]$. q is set to 0.7 based on our ablation study in Fig. 3.

To further improve the quality of the images and reduce the influence of noisy training data as much as possible, we provide Cross-View Matching (CVM) loss to achieve higher quality. The output of the IVE module is divided into K blocks with a size of 16×16 . As presented in Fig. 1, for each block δ_j in the output of the IVE module, the first step is to find its n most similar blocks from other regions. We set $n = 4$ empirically in our experiments. We then compute a weighted block p_j based on the similarities between δ_j and the identified n blocks:

$$p_j = \sum_{i=1}^n \frac{\frac{1}{MSE(\delta_j, s_i) + \iota}}{\sum_{k=1}^n \frac{1}{MSE(\delta_j, s_k) + \iota}} s_i, \quad (3)$$

where $s_i, i \in \{1, \dots, n\}$ denotes the i^{th} similar blocks, and ι is a small parameter to keep computational stability.

Integrating Eq. (2) and Eq. (3), we propose to compute a CVM loss:

$$L_{CVM} = \frac{1}{K} \sum_{j=1}^K \frac{(\|p_j - \sigma_j^g\|^2 + \epsilon)^q - 1}{q}, \quad (4)$$

where σ_j^g denotes the ground truth label for block δ_j .

Noise-to-Noise Training In practice, gold ground truth label σ^g is not available. We use noisy label σ_j in the training. We have:

$$\sigma_j = \sigma_j^g + n_j \quad (5)$$

The actual loss function based on Eq. (4) would be:

$$L_{CVM}^* = \frac{1}{K} \sum_{j=1}^K \frac{(\|p_j - \sigma_j\|^2 + \epsilon)^q - 1}{q} \quad (6)$$

The item $\|p_j - \sigma_j\|^2$ in Eq. (6) is further expanded to:

$$\|p_j - \sigma_j\|^2 = \|p_j - \sigma_j^g - n_j\|^2 = \|p_j - \sigma_j^g\|^2 - 2n_j^T p_j + (n_j^T n_j - 2n_j^T \sigma_j^g), \quad (7)$$

where the first term in Eq. (7) is the same term as in Eq. (4), and the third term is irrelevant to the model parameter. The second term has been proved to approximate 0 when computing the mean value according to the Lindeberg-Levy central limit theorem [12, 4].

Table 1: Comparison of OCTA imaging methods. The best result is colored by red, and the second-best result is colored by blue.

Methods	PSNR(dB) \uparrow	SSIM($\%$) \uparrow	CNR \uparrow
OMAG[26]	31.37 ± 0.53	84.03 ± 0.36	9.2
Unet[22]	27.58 ± 0.23	79.41 ± 0.11	8.5
Pix2Pix[10]	30.97 ± 0.12	85.41 ± 0.16	10.7
Swin-Tiny[19]	30.55 ± 0.14	83.30 ± 0.07	9.4
VQ-I2I[3]	31.03 ± 0.22	85.79 ± 0.19	10.1
Jiang’s Method[12]	32.97 ± 0.36	88.54 ± 0.38	12.4
Ours	34.61 ± 0.11	91.02 ± 0.18	15.8

Based on these derivation procedure, we have the formula:

$$\operatorname{argmin} \frac{1}{K} \sum_{j=1}^K \frac{(\|p_j - \sigma_j\|^2 + \epsilon)^q - 1}{q} = \operatorname{argmin} \frac{1}{K} \sum_{j=1}^K \frac{(\|p_j - \sigma_j^g\|^2 + \epsilon)^q - 1}{q}, \quad (8)$$

which indicates that the training with noisy data has similar output to the training with high quality ground truth data.

2.3 Implementation Details

The experiments are carried out on our local dataset. Due to the impossibility to obtain an ideal ground truth in OCTA, we compute pseudo high quality images and pseudo noisy label based on the OMAG algorithm with the input of 1,000 consecutive samples and 100 consecutive samples, respectively. The former are used for evaluation and the latter are used for training. We employ pretrained Swin-Unet to initialize the backbone in ICENet. The input of ICENet are 4 consecutive B-scan images. Each sample is resized to 896×896 and divided into 56×56 blocks with the size of 16×16 . The initial learning rate is 0.0002, which gradually decreases with the progress of the training. We used 4 NVIDIA Geforce RTX 2080Ti GPUs, and the batch size for each GPU is 4.

3 Experimental Results

3.1 Dataset and Evaluations

We use a Cirrus Angioplex SD-OCT (Carl Zeiss Meditec, Inc, Dublin, CA) with access to the raw data for data collection. We first collect repeated B-scans from rodents and monkeys using the machine, together with the corresponding regular OCTA scans. In the imaging, the animals are sedated using a ketamine and xylazine cocktail. Vital signals, including heart rate and respiration rate are continuously monitored throughout the imaging sessions. The animals are placed in a prone position with their head restrained stereotaxically. Note that

Table 2: The ablation studies for the proposed Intra-View Enhancement (IVE) module and the Cross-View Matching (CVM) loss.

IVE	CVM	PSNR(dB) \uparrow	SSIM(%) \uparrow
\times	\times	33.09 ± 0.14	88.23 ± 0.08
\checkmark	\times	33.84 ± 0.10	90.06 ± 0.15
\checkmark	\checkmark	34.61 ± 0.11	91.02 ± 0.18

movement of the animal is minimal during the entire imaging period, such that the OCTA B-scans are well aligned.

A total of 200 B-scan sets are collected from various locations, each consisting of 1,000 B-scans stored as 1000×1024 PNG images. Based on these repeated B-scan OCT images, we compute the corresponding pseudo ground truth for each location by the OMAG algorithm. Among these, 173 sets are designated for training, with the remainder allocated for testing. To quantitatively show the performance of our approach, we compute the peak signal-to-noise ratio (PSNR), structural similarity (SSIM) [28] and contrast-to-noise (CNR) [9] as the evaluation metrics.

3.2 Comparison Experiments

To evaluate the proposed ICENet, we compare it with two convolution-based baselines: Unet [22] and Pix2Pix [10]; two transformer-based baselines: Swin-Tiny [19], VQ-I2I [3]; one traditional medical image translation method: OMAG [26]; and one weakly supervised learning-based algorithm: Jiang’s method [12].

Quantitative results are provided in Table 1 to compare the performance between the proposed method and other algorithms. Each evaluation follows the same experimental settings, with 4 OCT repeated samples input. As shown in the table, all learning-based methods demonstrate a higher variance than traditional computation. The proposed method outperforms the second best method with a 4.97% higher PSNR, 2.80% higher SSIM, and 27.42% higher CNR. We provide visualization results in Fig. 2. By comparing all the results, it is noteworthy that our pipeline can enhance the image effectively, meanwhile preserving details.

3.3 Ablation Study

To evaluate the effectiveness of the proposed IVE module and CVM loss function, we train different variants with the same backbone. As shown in Table 2, IVE leads to 2.27% higher PSNR. When incorporating both modifications together, the PSNR witness to an increase of 4.59%. Regarding SSIM, the two variants show improvements of 2.07% and 3.16%, respectively.

We further perform ablation study for parameter q in Eq. (4). The results in Fig. 3 shows that our model achieves the best performance when setting q to 0.7, which is fixed in all other experiments mentioned in our work.

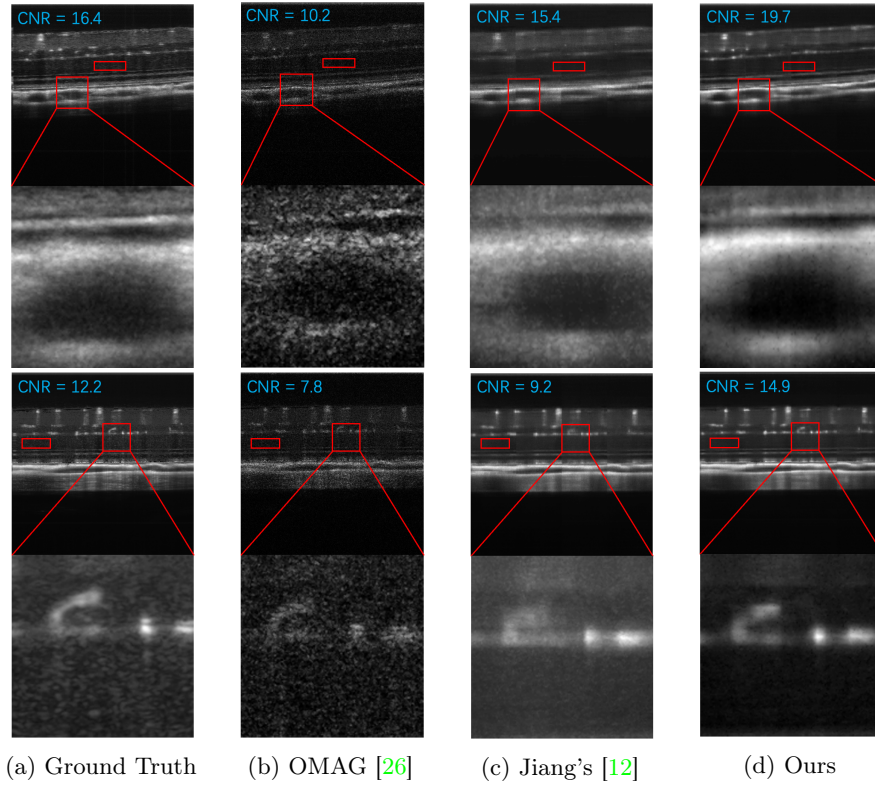


Fig. 2: Samples of OCTA Imaging. (a) the pseudo ground truth from 1000 overlapping scan (b) the results by regular OMAG by current commercial machine (c) the results by Jiang’s method and (d) our results.

4 Conclusion

In this work, we propose an intra- and cross-view enhancement pipeline for OCTA imaging, which computes OCTA from consecutive B-scans. Experimental results demonstrate that with limited repeated B-Scan input, our approach outperforms baseline learning-based OCTA imaging methods. The ablation results also demonstrate that the proposed IVE module and the CVM loss function help the network mitigate the negative influence of noisy labels. Compared with other algorithm, it provides a 4.97% higher PSNR, 2.80% higher SSIM, and 27.42% higher CNR. The findings suggest that the proposed pipeline serves as an effective solution to improve the clinical efficiency and quality of OCTA imaging.

Acknowledgments. This work is supported by the Agency for Science, Technology and Research under its MTC Programmatic Fund M23L7b0021 and AI³ Horizontal Technology Coordinating Office Grant C231118001.

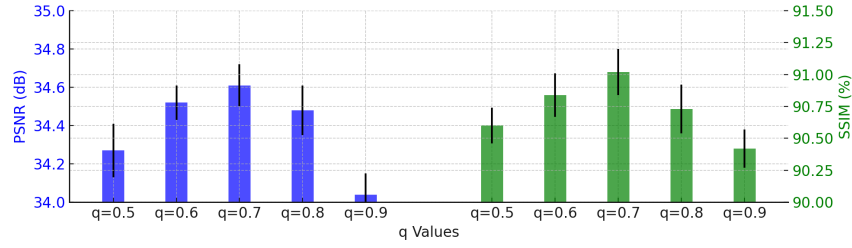


Fig. 3: The ablation study on different values of parameter q in Eq. (4). We follow the setting with the best result to conduct other experiments.

Disclosure of Interests. The authors have no competing interests to declare that are relevant to the content of this article.

References

1. Barron, J.T.: A general and adaptive robust loss function. In: CVPR. pp. 4331–4339 (2019) 4
2. Cao, H., Wang, Y., Chen, J., Jiang, D., Zhang, X., Tian, Q., Wang, M.: Swin-unet: Unet-like pure transformer for medical image segmentation. In: ECCV. pp. 205–218. Springer (2022) 3
3. Chen, Y.J., Cheng, S.I., Chiu, W.C., Tseng, H.Y., Lee, H.Y.: Vector quantized image-to-image translation. In: ECCV. pp. 440–456. Springer (2022) 6, 7
4. Cui, J., Gong, K., Guo, N., Wu, C., Meng, X., Kim, K., Zheng, K., Wu, Z., Fu, L., Xu, B., et al.: Pet image denoising using unsupervised deep learning. *European journal of nuclear medicine and molecular imaging* **46**, 2780–2789 (2019) 5
5. Danielyan, A., Katkovnik, V., Egiazarian, K.: Bm3d frames and variational image deblurring. *IEEE TIP* **21**(4), 1715–1728 (2011) 4
6. Enfield, J., Jonathan, E., Leahy, M.: In vivo imaging of the microcirculation of the volar forearm using correlation mapping optical coherence tomography (cmoct). *Biomedical optics express* **2**(5), 1184–1193 (2011) 2
7. Gao, S.S., Jia, Y., Zhang, M., Su, J.P., Liu, G., Hwang, T.S., Bailey, S.T., Huang, D.: Optical coherence tomography angiography. *Investigative Ophthalmology & Visual Science* **57**(9), OCT27–OCT36 (07 2016) 1
8. Ge, C., Yu, X., Yuan, M., Fan, Z., Chen, J., Shum, P.P., Liu, L.: Self-supervised self2self denoising strategy for oct speckle reduction with a single noisy image. *Biomedical Optics Express* **15**(2), 1233–1252 (2024) 2
9. Geissler, A., Gartus, A., Foki, T., Tahamtan, A.R., Beisteiner, R., Barth, M.: Contrast-to-noise ratio (cnr) as a quality parameter in fmri. *Journal of Magnetic Resonance Imaging: An Official Journal of the International Society for Magnetic Resonance in Medicine* **25**(6), 1263–1270 (2007) 7
10. Isola, P., Zhu, J.Y., Zhou, T., Efros, A.A.: Image-to-image translation with conditional adversarial networks. In: CVPR. pp. 1125–1134 (2017) 6, 7
11. Jia, Y., Tan, O., Tokayer, J., Potsaid, B., Wang, Y., Liu, J.J., Kraus, M.F., Subhash, H., Fujimoto, J.G., Hornegger, J., et al.: Split-spectrum amplitude-decorrelation angiography with optical coherence tomography. *Optics express* **20**(4), 4710–4725 (2012) 2

12. Jiang, Z., Huang, Z., Qiu, B., Meng, X., You, Y., Liu, X., Geng, M., Liu, G., Zhou, C., Yang, K., et al.: Weakly supervised deep learning-based optical coherence tomography angiography. *IEEE Transactions on Medical Imaging* **40**(2), 688–698 (2020) [2](#), [5](#), [6](#), [7](#), [8](#)
13. Lee, C.S., Tying, A.J., Wu, Y., Xiao, S., Rokem, A.S., DeRuyter, N.P., Zhang, Q., Tufail, A., Wang, R.K., Lee, A.Y.: Generating retinal flow maps from structural optical coherence tomography with artificial intelligence. *Scientific reports* **9**(1), 5694 (2019) [2](#)
14. Li, G., Wang, K., Dai, Y., Zheng, D., Wang, K., Zhang, L., Kamiya, T.: Physics-based optical coherence tomography angiography (octa) image correction for shadow compensation. *IEEE Transactions on Biomedical Engineering* (2024) [2](#)
15. Li, S., Zhang, D., Li, X., Ou, C., An, L., Xu, Y., Yang, W., Zhang, Y., Cheng, K.T.: Vessel-promoted oct to octa image translation by heuristic contextual constraints. *Medical Image Analysis* p. 103311 (2024) [2](#)
16. Liu, G., Jia, Y., Pechauer, A.D., Chandwani, R., Huang, D.: Split-spectrum phase-gradient optical coherence tomography angiography. *Biomedical Optics Express* **7**(8), 2943–2954 (2016) [2](#)
17. Liu, H., Lin, S., Ye, C., Yu, D., Qin, J., An, L.: Using a dual-tree complex wavelet transform for denoising an optical coherence tomography angiography blood vessel image. *OSA Continuum* **3**(9), 2630–2645 (2020) [2](#)
18. Liu, X., Huang, Z., Wang, Z., Wen, C., Jiang, Z., Yu, Z., Liu, J., Liu, G., Huang, X., Maier, A., et al.: A deep learning based pipeline for optical coherence tomography angiography. *Journal of Biophotonics* **12**(10), e201900008 (2019) [2](#)
19. Liu, Z., Lin, Y., Cao, Y., Hu, H., Wei, Y., Zhang, Z., Lin, S., Guo, B.: Swin transformer: Hierarchical vision transformer using shifted windows. In: *CVPR*. pp. 10012–10022 (2021) [6](#), [7](#)
20. Ma, Y., Yan, Q., Liu, Y., Liu, J., Zhang, J., Zhao, Y.: Strunet: Perceptual and low-rank regularized transformer for medical image denoising. *Medical Physics* **50**(12), 7654–7669 (2023) [2](#)
21. Moran, N., Schmidt, D., Zhong, Y., Coady, P.: Noisier2noise: Learning to denoise from unpaired noisy data. In: *CVPR*. pp. 12064–12072 (2020) [2](#), [3](#)
22. Ronneberger, O., Fischer, P., Brox, T.: U-net: Convolutional networks for biomedical image segmentation. pp. 234–241. Springer (2015) [6](#), [7](#)
23. Rousseeuw, P.J., Leroy, A.M.: Robust regression and outlier detection. John Wiley & sons (2005) [4](#)
24. Schottenhamml, J., Würfl, T., Ploner, S.B., Husvagt, L., Hohberger, B., Fujimoto, J.G., Maier, A.: Ssn2v: unsupervised oct denoising using speckle split. *Scientific Reports* **13**(1), 10382 (2023) [3](#)
25. Song, H., Kim, M., Park, D., Shin, Y., Lee, J.G.: Learning from noisy labels with deep neural networks: A survey. *IEEE transactions on neural networks and learning systems* **34**(11), 8135–8153 (2022) [3](#)
26. Wang, R.K.: Optical microangiography: a label-free 3-d imaging technology to visualize and quantify blood circulations within tissue beds in vivo. *IEEE Journal of Selected Topics in Quantum Electronics* **16**(3), 545–554 (2009) [2](#), [6](#), [7](#), [8](#)
27. Wang, R.K., An, L., Saunders, S., Wilson, D.J.: Optical microangiography provides depth-resolved images of directional ocular blood perfusion in posterior eye segment. *Journal of biomedical optics* **15**(2), 020502–020502 (2010) [2](#)
28. Wang, Z., Bovik, A.C., Sheikh, H.R., Simoncelli, E.P.: Image quality assessment: from error visibility to structural similarity. *IEEE transactions on image processing* **13**(4), 600–612 (2004) [7](#)

29. Xu, Y., Xu, X., Jin, L., Gao, S., Goh, R.S.M., Ting, D.S.W., Liu, Y.: Partially-supervised learning for vessel segmentation in ocular images. In: MICCAI 2021. pp. 271–281. Springer International Publishing, Cham (2021) [1](#)
30. Yang, J., Hu, Y., Fang, L., Cheng, J., Liu, J.: Universal digital filtering for denoising volumetric retinal oct and oct angiography in 3d shearlet domain. *Optics Letters* **45**(3), 694–697 (2020) [2](#)
31. Yu, L., Chen, Z.: Doppler variance imaging for three-dimensional retina and choroid angiography. *Journal of biomedical optics* **15**(1), 016029–016029 (2010) [2](#)
32. Zhang, Y., Li, J., Liu, C., Zheng, K., Zhang, B., Zhou, Y., Dai, C., Fan, S., Yao, Y., Zhuang, R., et al.: Development of a multi-scene universal multiple wavelet-fft algorithm (mw-fft) for denoising motion artifacts in oct-angiography in vivo imaging. *Optics Express* **30**(20), 35854–35870 (2022) [2](#)
33. Zhang, Z., Sabuncu, M.: Generalized cross entropy loss for training deep neural networks with noisy labels. *NeurIPS* **31** (2018) [4](#)
34. Zhang, Z., Ji, Z., Chen, Q., Yuan, S., Wen, F.: Texture-Guided U-Net for OCT-to-OCTA Generation, pp. 42–52. *Pattern Recognition and Computer Vision, 4th Chinese Conference, PRCV 2021, Beijing, China* (10 2021) [2](#)